JMEPEG (2023) 32:9765–9776
https://doi.org/10.1007/s11665-023-07831-7

1059-9495/$19.00

TECHNICAL ARTICLE

Influence of Manganese Content on Microstructure, Mechanical Properties and High Temperature Oxidation Resistance of Reduced Activation Ferritic/Martensitic Steels

Wen Zeng, Ming Zhou, Mei Yang, Risheng Qiu, Xinu Tan, Anruo Zhou, and Xianfu Luo

Submitted: 13 October 2022 / Revised: 15 December 2022 / Accepted: 23 December 2022 / Published online: 6 April 2023

The effect of the manganese content (0.5-2.0 wt.%) on the microstructure, mechanical properties and high temperature oxidation resistance of reduced activation ferritic/martensitic (RAFM) steels was studied. The examinations reveal that the microstructure of the steels shows a fully martensite structure. A large number of $M_{23}C_6$ carbides and a small number of Zr(C, N) carbonitrides were detected in the steels. The results of mechanical experiments showed that the strength increases and the toughness decreases with increasing Mn content. The improvement of strength can be ascribed to solution strengthening by Mn and gain size strengthening by refining lath width. After oxidation at 650 °C for 400 h, both $MnCr_2O_4$ oxides and Cr_2O_3 oxides are founded on the surface of the steels. The steel with 1.2 wt.% Mn exhibit the optimum high temperature oxidation resistance, followed by the steel with 0.5 wt.% Mn. The increase of oxidation resistance can be ascribed to the addition of Mn promotes the formation of Mn oxides, which refined the diameter of $MnCr_2O_4$ oxides. The decrease of oxidation resistance mainly due to the higher Mn content reduces the critical concentration of Cr to form Cr oxides (Cr_2O_3), thus promoting the formation of large-sized Cr_2O_3 oxides.

Keywords ferritic/martensitic steel, manganese, mechanical property, microstructure, oxidation resistance

1. Introduction

The generation IV nuclear reactors are characterized by economics, safety, reliability, proliferation resistance, physical protection and sustainability (Ref 1). However, the generation IV nuclear reactors have higher outlet temperature, higher radiation dose and extreme corrosion environment compared with the previous generation reactors (Ref 1). Therefore, structure materials with higher performance are needed for the generation IV nuclear reactors. Reduced activation ferritic/martensitic (RAFM) steels are considered as the candidate material for the generation IV nuclear reactors due to their low coefficient of thermal expansion, good thermal conductivity, excellent creep resistance and oxidation resistance (Ref 2). The microstructure of RAFM steels at room temperature is fully martensite or martensite with a small number of ferrite. RAFM steels also contain a large number of precipitates, such as $M_{23}C_6$ carbide (M = Cr, Fe, W), MX phase (M = V, Ta; X = C, N) and *Z* phase (Ref 3-5). The $M_{23}C_6$ carbide and MX phase impede dislocations movement and play a role in precipitation strengthening, while MX phase is more stable than $M_{23}C_6$ carbide at high temperature (Ref 6, 7). In addition to precipitation strengthening, the strengthening mechanisms of RAFM steels also include solid solution strengthening, dislocation strengthening and grain boundary strengthening (Ref 8, 9).

Mn is one of the usually used alloying elements in steels, which has a strong influence on the inclusions, mechanical properties and microstructure of steels. Mn has a strong ability of deoxidation and desulfurization in steels. It can combine with S to form MnS and eliminate the harmful effects of S (Ref 10). And it can combine with O to form MnO and reduce the O content in steels (Ref 11). Besides, Mn can improve the hardness, strength and wear resistance of steels (Ref 12, 13). The increased Mn content in high-C and high-Mn austenitic steels enhances the stacking fault energy and promotes the formation of deformation twins and work hardening characteristic, thus improving the strength and plasticity of the steels (Ref 13). Furthermore, Mn can also affect the microstructure of steels. The average grain size of high silicon alloyed non-oriented electrical steels decreases as Mn content increases (Ref 14). The addition of Mn in Fe-NiAl steels accelerates the

Wen Zeng, School of New Energy and Materials, Southwest Petroleum University, Chengdu 610500 Sichuan, China; School of Materials Science and Engineering, Chongqing University, Chongqing 400044, China; and School of Metallurgy and Materials Engineering, Chongqing University of Science and Technology, Chongqing 401331, China; **Ming Zhou** and **Mei Yang**, School of New Energy and Materials, Southwest Petroleum University, Chengdu 610500 Sichuan, China; and **Risheng Qiu** and **Xinu Tan**, School of Materials Science and Engineering, Chongqing University, Chongqing 400044, China; **Anruo Zhou** and **Xianfu Luo**, School of Metallurgy and Materials Engineering, Chongqing University of Science and Technology, Chongqing 401331, China. Contact e-mails: mr.zhouming@163.com and rsqiu@cqu.edu.cn.

precipitation of NiAl nanoparticles, which increases the hardness and shortens the time to reach the peak hardness (Ref 15). The addition of Mn in Fe-Cu-Ni-Al steels enhanced the effect of precipitation hardening at early aging and accelerated the whole process of precipitation hardening (Ref 16).

Mn in RAFM steels is often used to control the Cr equivalent (Ref 17). It can expand austenite area and avoid the formation of δ-ferrite during the austenitization heat treatment (Ref 18). The δ-ferrite is harmful for tensile and Charpy impact properties of RAFM steels (Ref 19-22). Furthermore, Mn is considered to reduce the M_S temperature, thus reducing the residual tensile stress in steels after thermal cycle processing (welding, additive manufacturing, etc.) (Ref 23). There are only a few studies on the effect of Mn on the properties of RAFM steels. Chen et al. (Ref 24, 25) found that Mn plays a key role in the oxide scale formation of RAFM steels, which promotes the formation of Mn oxides on the surface of steels and improves the compactness of oxide scale. Jin et al. (Ref 26) found that the high temperature oxidation resistance of RAFM steels is improved as the content of Mn increased from 0.04-0.93 wt.%. And the mechanical properties of RAFM steels with different Mn content have no obvious difference (Ref 26). Dong et al. (Ref 27) found that increasing the Mn content in ferritic/martensitic steels reduced the corrosion resistance of ferritic/martensitic steels in supercritical water (SCW). As can be seen, quantitative and systematic studies on the effect of Mn on the microstructure, mechanical properties and high temperature oxidation resistance of RAFM steels are still rare.

In this work, RAFM steels with Mn contents in the range of 0.5-2.0 wt.% were designed. A systematic study of Mn on the microstructure, mechanical properties and high temperature oxidation resistance of RAFM steels were conducted. The correlation between properties and microstructure were presented.

2. Experimental

The chemical compositions of RAFM steels with various Mn contents are given in Table 1. The RAFM steels with 0.5, 1.2 and 2.0 wt.% Mn are named 0.5Mn, 1.2Mn and 2.0Mn, respectively. The RAFM steels were prepared by the vacuum induction melting method, followed by hot-forging into a 45 × 60 mm plate. Subsequently, the hot-forged plates were hot-rolled to 8-mm-thick plate at temperatures between 950 and 1100 °C. In order to obtain the steels with the best performance, normalizing experiments at different normalizing temperatures (950, 980, 1010, 1040, 1070 °C) were carried out on the hot-rolled 0.5Mn steel. After normalizing, the steels were tempered at 760 °C for 90 min.

Cubic samples with the dimension of 2.5 × 10 × 30 mm^3 were used for high temperature oxidation resistance test. The surfaces of the rectangular samples were ground to 2000 grit using SiC and polished using diamond polishing paste. The polished samples were cleaned by ultrasonic cleaning in ethanol and then drying. High temperature oxidation is carried out in a muffle furnace with air atmosphere, and the oxidation temperature is 650 °C. The samples were taken out at 50, 100, 200, 300 and 400 h, respectively, and weighed discontinuously to obtain the oxidation weight gain curves. The total oxidation time is 400 h.

In terms of the mechanical properties, tensile and hardness tests at room temperature were performed. For tensile test, samples with a gauge section of 5 mm in diameter and 25 mm in length were tested at a crosshead rate of 1 mm/min at room temperature using a universal tensile test machine (Shimadzu AG-X plus Series, Japan) for tensile teste. Standard V-notch Charpy impact specimens with the size of 10 × 5 × 55 mm were subjected to the impact test at room temperature. Three samples of each type RAFM steels were evaluated in tensile test and Charpy impact test. The hardness test was performed by a Vickers hardness tester (HVS-1000Z) with loading force of 500 g for 10 s, and the obtained hardness values were the average of 10 measurements.

The analysis of the microstructure and precipitates was performed using scanning electron microscope (SEM, HITACHI S-3700 N, Japan) and transmission electron microscope (TEM, TECNAI G2 F20, USA). The SEM samples were mechanically polished and etched with 1% solution (5 g $FeCl_3$ + 50 mL HCl + 100 mL H_2O) for 1 min. The TEM samples were obtained by jet polishing in a solution of 90% C_2H_5OH and 10% $HClO_4$ at − 30 °C and 20 V. The phase compositions of oxides on the surface of RAFM steels after oxidation were analyzed with an x-ray diffraction (XRD, Rigaku smartLab-9, Japan) by Cu Kα radiation (45 kV, 200 mA).

3. Results and Discussion

3.1 Optimization of Normalizing Temperature

Figure 1 shows the hardness of 0.5Mn steel after normalized at different temperatures. It is obvious that the hardness of 0.5Mn steel normalized at 950-1010 °C is lower than 200 HV. The hardness of 0.5Mn steel normalized at 1040 °C is the highest (225 ± 2 HV), and the hardness decreased as the normalizing temperature increased to 1070 °C.

In order to analyze the reason for the evolution of hardness with normalizing temperature, the microstructure of 0.5Mn steel with different normalizing temperature was investigated by SEM. Figure 2 shows the microstructure of 0.5Mn steel

Table 1 Chemical compositions of the investigated RAFM steels (wt.%)

Steels	C	Cr	W	Si	V	Zr	N	Ti	Mn	Fe
0.5Mn	0.18	10.5	1.5	0.6	0.2	0.2	0.04	0.01	0.5	Bal
1.2Mn	0.18	10.5	1.5	0.6	0.2	0.2	0.04	0.01	1.2	Bal
2.0Mn	0.18	10.5	1.5	0.6	0.2	0.2	0.04	0.01	2.0	Bal

after normalized at different temperature. It can be found that the microstructure of 0.5Mn steels normalized at 950-1010 °C is composed of martensite and ferrite, while the 0.5Mn steels normalized at 1040 and 1070 °C is a fully martensite structure. It is known that the hardness of martensite is higher than that of ferrite. Therefore, the hardness of 0.5Mn steels normalized at 1040 and 1070 °C is higher than 0.5Mn steels normalized at 950-1010 °C. Furthermore, the hardness decreased as normalizing temperature increased from 1040 to 1070 °C. This is mainly due to the coarsening of martensite lath with increasing austenitizing temperature (Ref 28). Therefore, in order to get a fully martensitic structure and optimum hardness, the normalizing temperature of 0.5Mn steel is selected as 1040 °C.

The addition of Mn will reduce the Ac3 temperature of ferritic/martensitic steels (Ref 26). Hence, 1.2Mn and 2.0Mn steels can obtain a fully martensite structure after normalizing at 1040 °C.

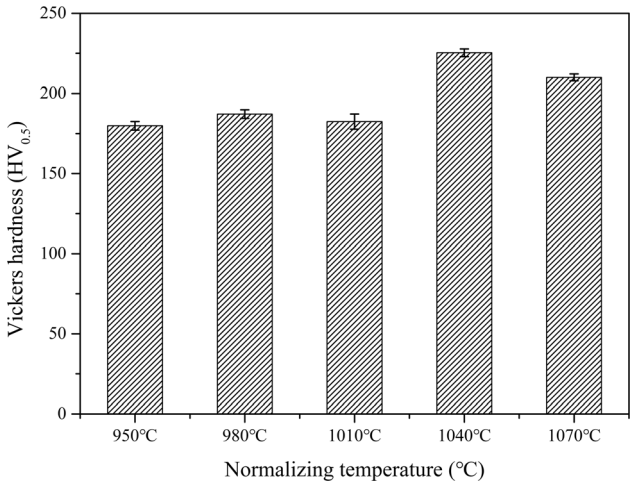

Fig. 1 Vickers hardness of 0.5Mn steel after normalized at different temperature

In order to study the effect of Mn content on the microstructure, mechanical properties and high temperature oxidation resistance of ferritic/martensitic steels, the normalizing temperature of 1.2Mn and 2.0Mn steels is also selected as 1040 °C.

3.2 Microstructure Characterization

Figure 3 shows the phase diagrams of 0.5, 1.2 and 2.0Mn steels obtained using Thermo-Calc with TCFE10 database. There are five types of precipitates in the steels, i.e., $M_{23}C_6$ carbides, Zr(C, N) carbonitrides, Laves phase, Z phase and σ phase. In this work, only $M_{23}C_6$ carbides and Zr(C, N) carbonitrides were present after heat treatment. Other precipitates have slow formation kinetics and usually require extended thermal aging. The Laves phase usually formed after long-term thermal aging, which will lead to creep strength failure (Ref 29). The Z phase also formed after long-term thermal aging, which does not contribute to strengthening and consume the MX particles during their growth, causing a breakdown in creep strength (Ref 30, 31). The σ phase is rare in RAFM steels, which typically formed at boundaries between δ-ferrite and martensite (Ref 32). The effect of σ phase on the mechanical properties of RAFM steels is generally considered to be deleterious (Ref 32). The fraction of $M_{23}C_6$ carbides and Zr(C, N) carbonitrides in 0.5Mn, 1.2Mn and 2.0Mn steels is predicted to be -4 and -0.3%, respectively.

The SEM microstructures of 0.5Mn, 1.2Mn and 2.0Mn steels are shown in Fig. 4. It is clear that the microstructures of the steels show a fully martensite structure. There are two sizes of precipitates. The larger-size precipitates are rare in steels, while the dimeter can be several microns. The smaller-size precipitates distribute along martensitic lath boundaries and prior austenite grain boundaries (PAGBs), which are probably the $M_{23}C_6$ carbides. The identification of smaller-size precipitates will be conducted by the following TEM analysis. The compositions of larger-size precipitates were analyzed by EDS. As shown in Fig. 4(d), the larger-size precipitates composed of

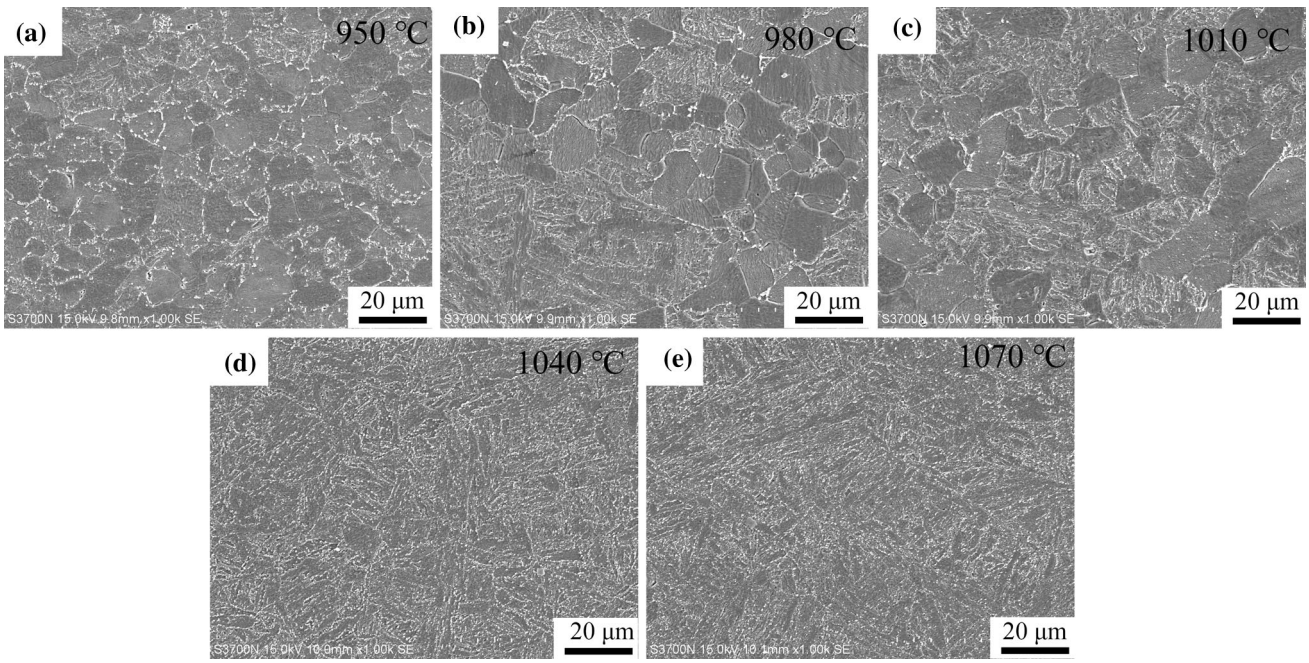

Fig. 2 SEM images of 0.5Mn steel after normalized at (a) 950 °C, (b) 980 °C, (c) 1010 °C, (d) 1040 °C and (e) 1070 °C

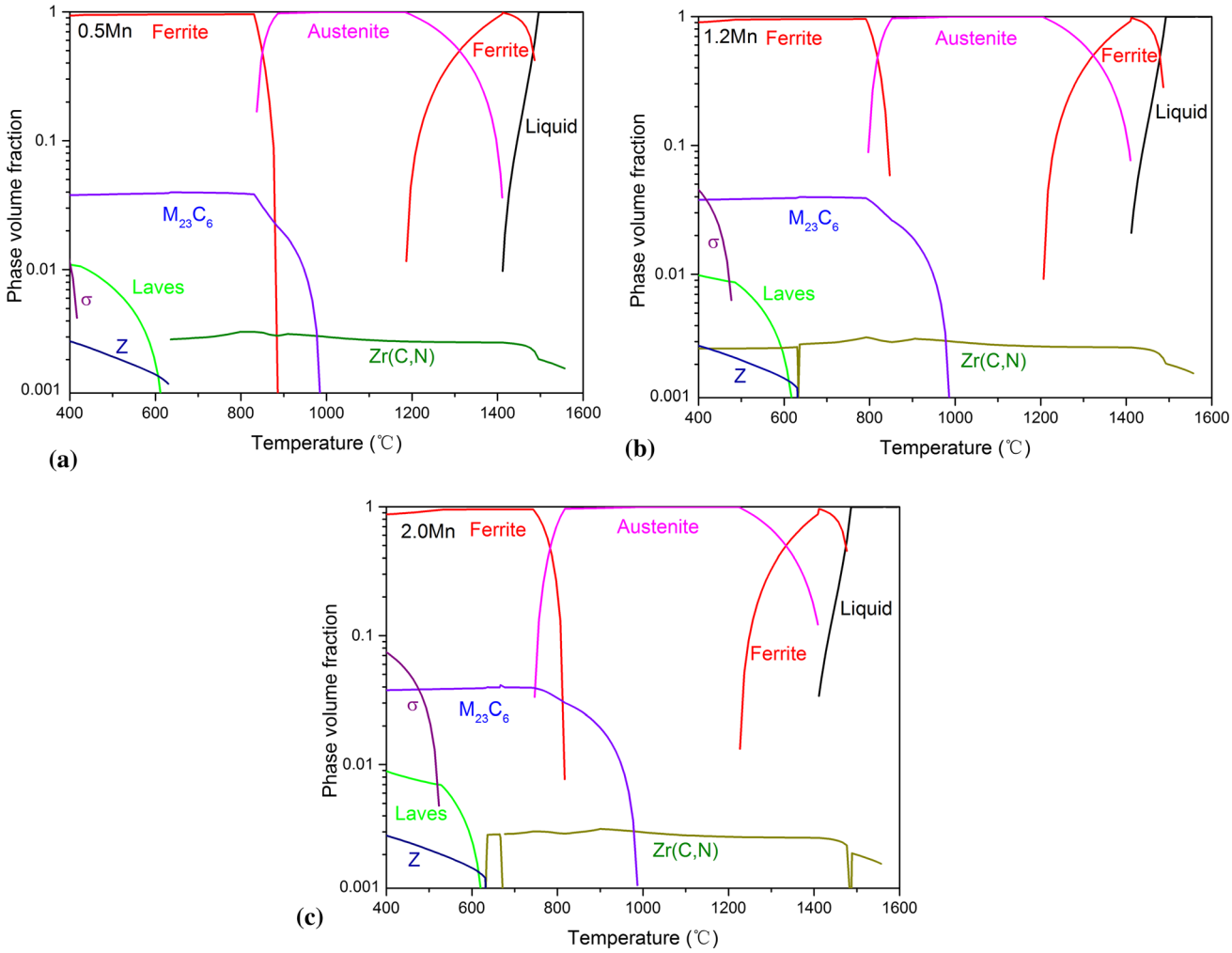

Fig. 3 Phase diagrams of (a) 0.5, (b) 1.2 and (c) 2.0Mn steels calculated by Thermo-Calc with TCFE10 database.

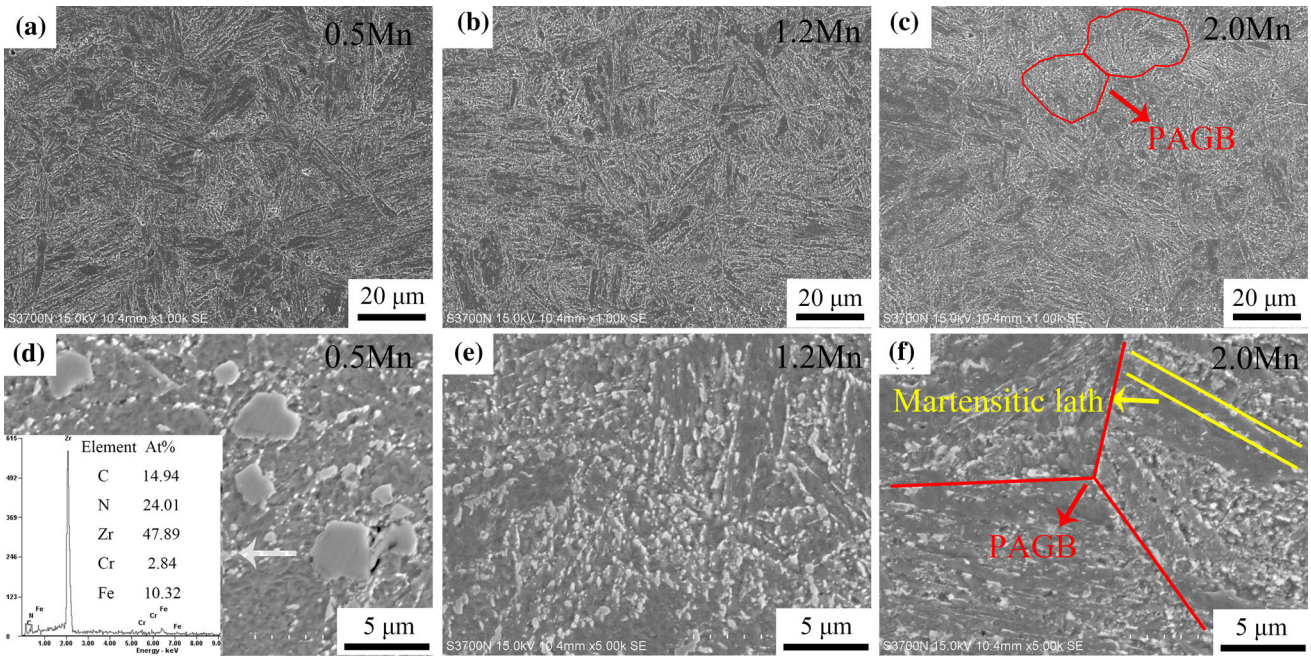

Fig. 4 SEM images of (a), (d) 0.5Mn steel, (b), (e) 1.2Mn steel and (c), (f) 2.0Mn steel normalized at 1040 °C and tempered at 760 °C.

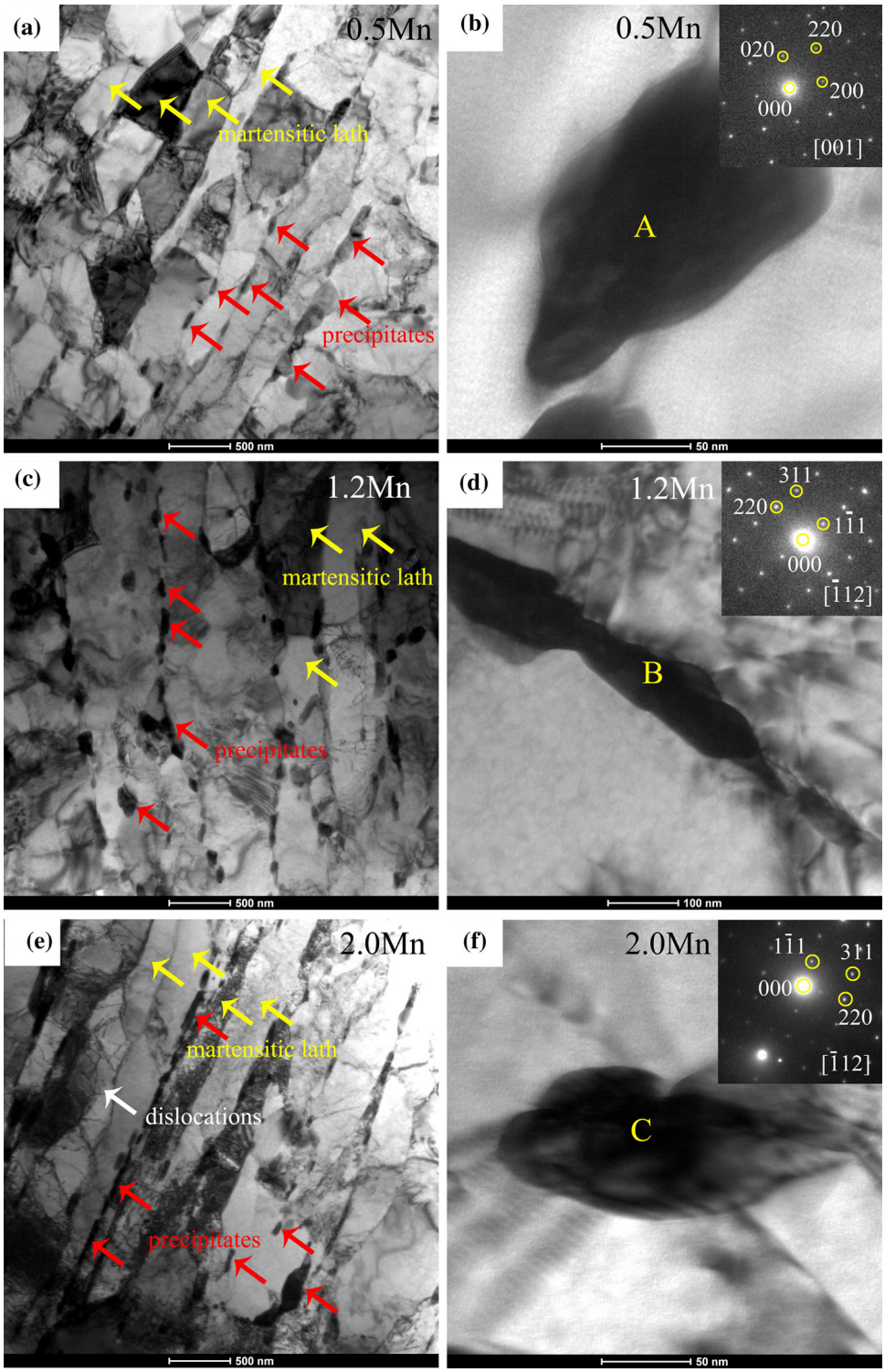

Fig. 5 TEM images of (a, b) 0.5Mn steel, (c, d) 1.2Mn steel and (e, f) 2.0Mn steel.

C, N, Zr, Cr and Fe, which corresponding to the Zr(C, N) carbonitrides in previous phases analysis. The Zr(C, N) carbonitrides is formed by ZrC and ZrN, which will precipitate when steels contains C and N (Ref 33).

In order to further analyze the martensitic lath and precipitates in the steels, TEM analysis was performed. The TEM microstructures of 0.5Mn, 1.2Mn and 2.0Mn steels are shown in Fig. 5. It is clear that the microstructure of the steels is composed of martensitic lath and precipitates. The precipitates distributed along martensitic lath boundaries, which have long strip and ellipse shape, as shown in Fig. 5(a), (c) and (e). In order to identify the precipitates, EDS analysis and selected area diffraction (SAD) analysis were employed. Figure 6 illustrates the EDS maps and mainly element compositions of the precipitates in the steels. It can be found that the precipitates are enriched in Cr, followed by Fe and W. Furthermore, the

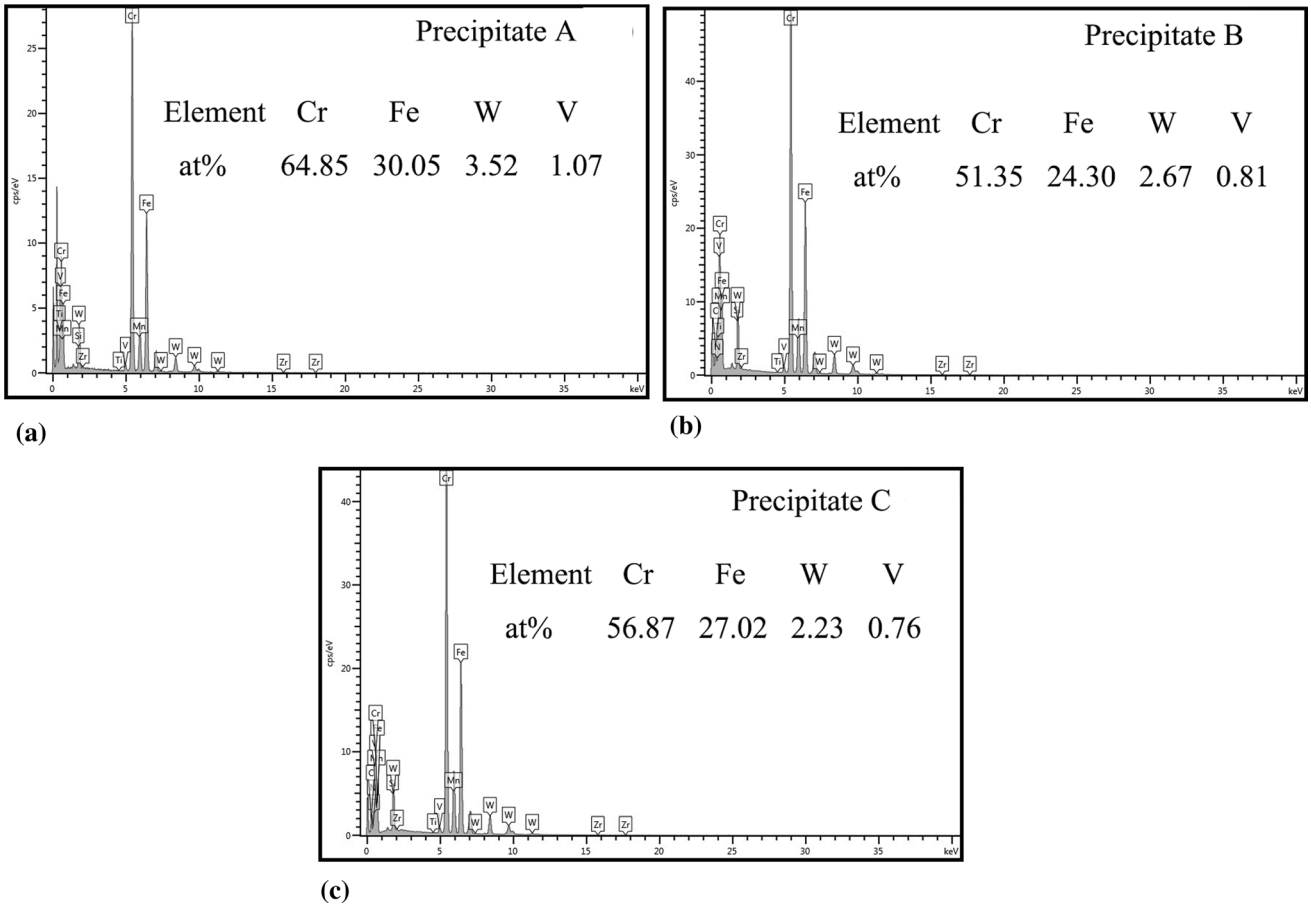

Fig. 6 The EDS analyses of precipitates in Fig. 5

SAD patterns of precipitates in Fig. 5(b), (d) and (e) are matched well with the diffraction patterns of $Cr_{23}C_6$. Therefore, it can be proved that the precipitates distributed along martensitic lath boundaries are $M_{23}C_6$ (M = Cr, Fe, W) carbides.

In order to uncover the effect of Mn on the tempered martensite and Cr-rich $M_{23}C_6$ precipitates, martensitic lath width and precipitates diameter in the RAFM steels were statistically analyzed, the results are shown in Fig. 7 and 8, respectively. The results of martensitic lath width and precipitates diameter were analyzed from five TEM photographs. It can be seen in Fig. 7 that the martensitic lath width in the steels is 100-500 nm. The average lath width (L_{ave}) of martensite in 0.5Mn, 1.2Mn and 2.0Mn steels is 296 ± 69, 300 ± 79 and 243 ± 69 nm, respectively. It can be found that the L_{ave} of 0.5Mn and 1.2Mn steel is similar, while the L_{ave} of 1.2Mn steel is significantly lower than that of other steels. However, there is no obvious difference in precipitates diameter between the steels, as depicted in Fig. 8. The diameter of precipitates in steels is mainly 50-200 nm. The average diameter (D_{ave}) of precipitates in 0.5Mn, 1.2Mn and 2.0Mn steels is 101 ± 45 nm, 122 ± 49 nm and 111 ± 48 nm, respectively. It can be concluded that the increase of Mn content can refine the martensitic lath of steels, but has little effect on the precipitation behavior. This was mainly because Mn tends to segregate to grain boundaries to lower its energy and induced the solute drag effect (Ref 14). The solute drag effect will confine the grain growth (Ref 34, 35).

3.3 Mechanical Properties

The mechanical properties of 0.5Mn, 1.2Mn and 2.0Mn steels are listed in Table 2. It is clear that the yield strength (YS, σ_s) and ultimate tensile strength (UTS, σ_b) of the steels increase with the increase of Mn content. The YS and UTS of 1.2Mn steel have a little increase compared with 0.5Mn steel, while 2.0Mn steel exhibits the highest YS (625.3 ± 14.0 MPa) and UTS (812.9 ± 4.9 MPa). The strength and toughness of steels are generally opposite. The total elongation (TE, E) of steels decreases with the increase of Mn content. Table 2 also lists the Vickers hardness and impact energy of the steels. The hardness of the steels has a little increase with increasing Mn content. Compared with the little variation of hardness, the impact property exhibits a significant variation. The impact energy of 0.5Mn, 1.2Mn and 2.0Mn steels at room temperature is 43.7 ± 1.7 J, 37.3 ± 0.9 J and 30.6 ± 1.2 J, respectively. The impact toughness of the steels decreases dramatically with the increase of Mn content.

The fracture surfaces of 0.5Mn, 1.2Mn and 2.0Mn steels after tensile test are shown in Fig. 9. It shows that the steels are fractured in a ductile manner and have a large number of dimples. It can be seen in Fig. 9(d) that there are larger-size particles in dimples, which are Zr(C, N) carbonitrides as analyzed previously. The fracture surfaces of steels after Charpy impact test are shown in Fig. 10. It can be found that the fracture surface of 2.0Mn steel is smooth compared with 0.5Mn and 1.2Mn steels. And there are cracks in the fracture surface of 2.0Mn steel, as depicted in Fig. 10(f), which

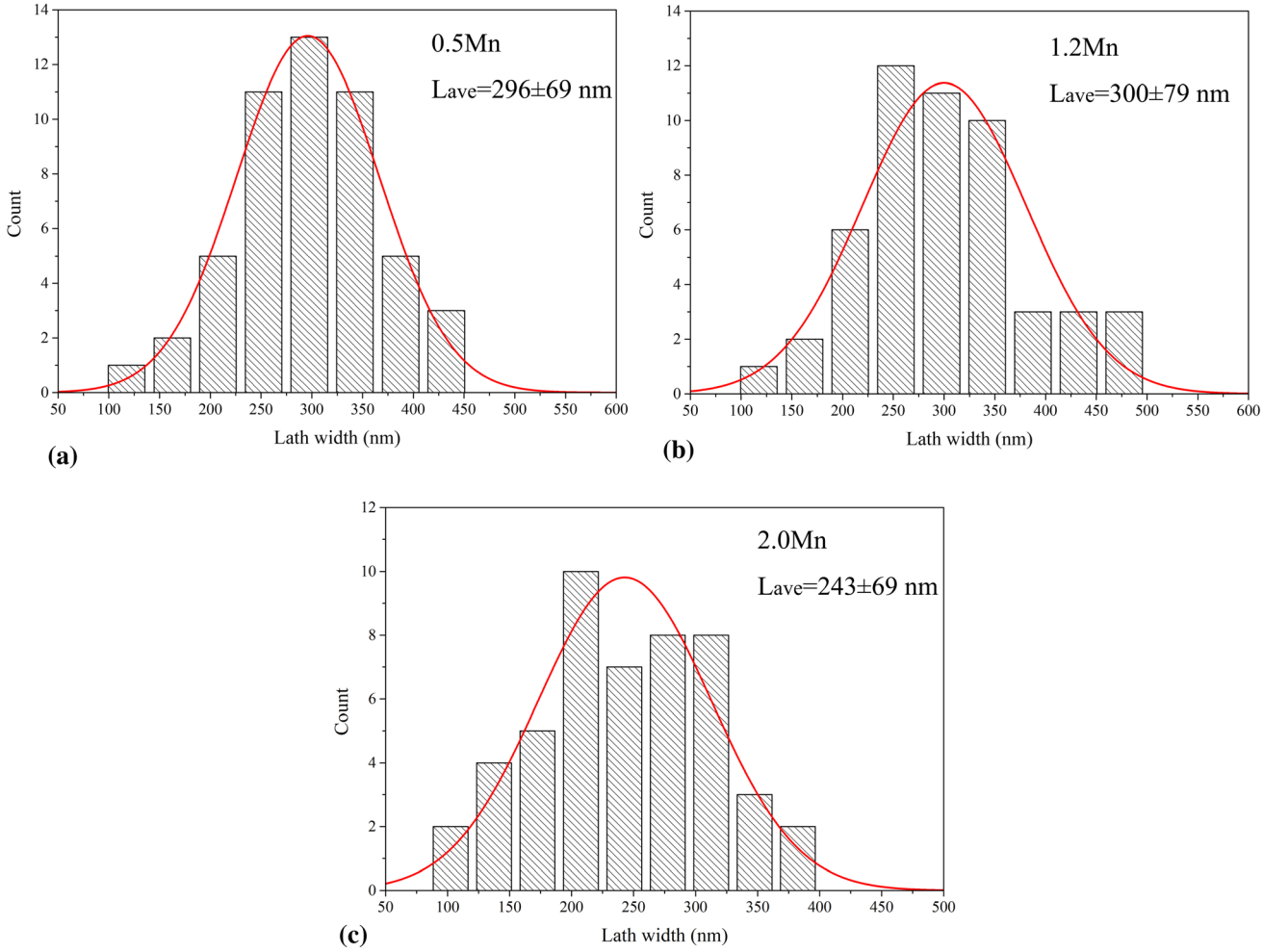

Fig. 7 The lath width distribution of martensite in (a) 0.5, (b) 1.2 and (c) 2.0Mn steels.

indicates the lower impact toughness. The results of fracture morphologies are in agreement with the mechanical properties of the steels.

The results show that the strength increases and the toughness decreases with the increase of Mn content. The yield strength (σ_s) of steels with primarily martensite and bainite can be estimated by (Ref 36):

$$\sigma_s = \sigma_{Fe} + \sigma_{ss} + \sigma_P + \sigma_L + \sigma_D \quad \text{(Eq 1)}$$

where σ_{Fe} represents the strength of annealed pure Fe, σ_{ss} represents the solid solution strengthening, σ_P represents the precipitation strengthening, σ_L represents the grain size strengthening (or grain boundary strengthening), here we use the lath size instead of grain size, σ_D represents the dislocation strengthening,

The solid solution hardening σ_{ss} can be estimated by (Ref 36):

$$\sigma_{ss} = 1723[C]^{1/2} + 105[Si] + 45[Mn] + 37[Ni] + 18[Mo] + 5.8[Cr] + 4.8[V] \quad \text{(Eq 2)}$$

where σ_{ss} in unit of MPa, all the elements [Z] are in weight percent.

The grain size strengthening σ_L can be estimated by (Ref 36):

$$\sigma_L = K_L \cdot L_{ave}^{-1} \quad \text{(Eq 3)}$$

where K_L represents the coefficient for strengthening due to lath size, $\sim$ 115 MPa, and L_{ave} represents the average lath width with units of μm.

As previous microstructure analysis, Mn has no significant effect on the precipitation behavior. Therefore, the effect of Mn content on the precipitation strengthening (σ_P) can be neglected. In addition, dislocations in RAFM steels are generally related to the produced process and some alloying elements (C and N) (Ref 37). As the same preparation process and alloying elements (except for Mn) among the RAFM steels, we consider that the dislocation strengthening σ_D of the RAFM steels is equivalent. Therefore, the strength variation of RAFM steels caused by Mn content is mainly attributed to solution strengthening and grain size strengthening (lath size strengthening). The toughness of the RAFM steels decreases with the increase of Mn content. This is mainly due to the effect of solution strengthening, which improves the strength and reduces the toughness of steels (Ref 38).

3.4 Oxidation Behavior

Figure 11 shows the weight gain curves of 0.5Mn, 1.2Mn and 2.0Mn steels oxidized at 650 °C up to 400 h. It is clear that 1.2Mn steel shows the lowest weight gain, followed by 0.5Mn steel and 2.0Mn steel. In other words, 1.2Mn steel shows the optimum high temperature oxidation resistance among the

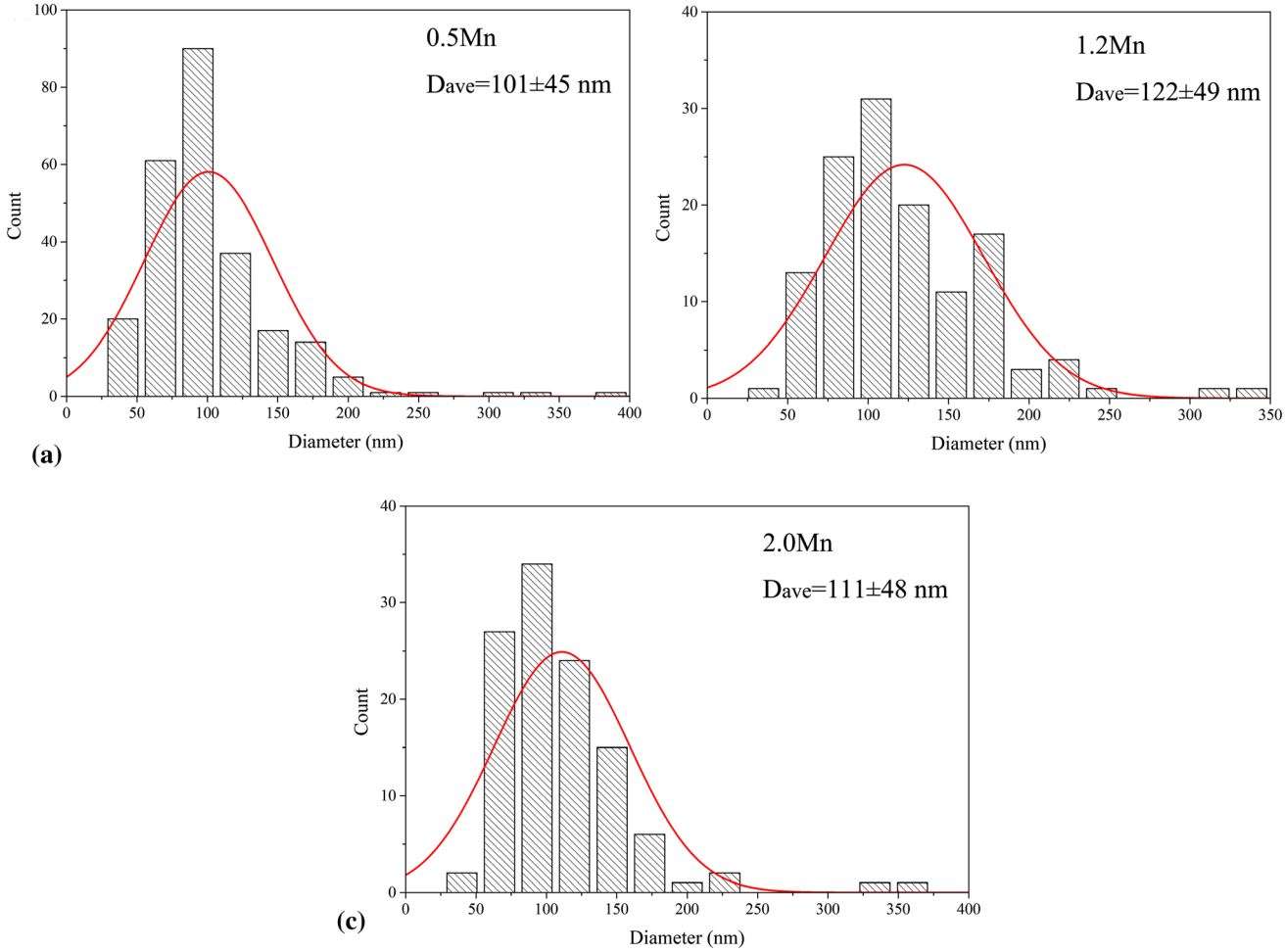

Fig. 8 The diameter distribution of precipitates in (a) 0.5, (b) 1.2 and (c) 2.0Mn steels.

Table 2 Tensile properties, Vickers hardness and impact energy of 0.5, 1.2 and 2.0Mn steels

Steels	YS , σ_s,MPa	UTS , σ_b, MPa	TE , E, %	Vickers hardness, $HV_{0.5}$	Impact energy, J
0.5Mn	585.3 ± 11.4	769.9 ± 0.9	25.1 ± 0.9	225.4 ± 2.4	43.7 ± 1.7
1.2Mn	590.6 ± 8.7	776.9 ± 5.7	21.0 ± 1.7	234.0 ± 2.2	37.3 ± 0.9
2.0Mn	625.3 ± 14.0	812.9 ± 4.9	20.1 ± 1.1	241.6 ± 2.7	30.6 ± 1.2

RAFM steels. Furthermore, the oxidation rate at 200-300 h is obviously higher than that of other times.

In order to determine the oxides on the surface of steels after oxidized at 650 °C, the XRD experiment has been carried out and the results are shown in Fig. 12. Two types of oxides were identified except for Fe-Cr matrix, namely Cr_2O_3 oxides and $MnCr_2O_4$ oxides. It is known that the intensity of the XRD peak can indicate the phase content. The higher the peak intensity is, the higher the phase content is. The intensity of $MnCr_2O_4$ phase in 0.5Mn steel is higher than that of Cr_2O_3 phase. Therefore, it can be concluded that the oxides on the surface of 0.5Mn steel is composed of a large number of $MnCr_2O_4$ oxides and a small number of Cr_2O_3 oxides. However, the intensity of $MnCr_2O_4$ phase and Cr_2O_3 phase of 2.0Mn steel is equivalent nearly. This indicates that the content of $MnCr_2O_4$ oxides and Cr_2O_3 oxides on the surface of 2.0Mn steel is equivalent nearly.

The morphologies of oxides layers of 0.5Mn, 1.2Mn and 2.0Mn steels oxidized at 650 °C for 400 h are shown in Fig. 13. It can be found that only granular oxides are formed on the surface of 0.5Mn steel, while there are both granular oxides and lamellar oxides on the surface of 1.2Mn steel and 2.0Mn steel. In addition, the number and size of lamellar oxides on the surface of 1.2Mn steel are smaller than that of 2.0Mn steel. The element compositions of lamellar oxides and granular oxides are analyzed by EDS, and the results are listed in Table 3. It can be found that the A, B and D particles are granular oxides, which have a similar elemental composition of ~ 50 at.% Cr, ~ 28 at.% Cr and ~ 20 at.% Mn. And the C and E particles are lamellar oxides, which have a similar elemental composition of ~ 50 at.% Cr, ~ 40 at.% Cr and ~ 10 at.% Mn. It should be noted that the compositions of lamellar oxides have a higher Cr content and a lower Mn content than that of granular oxides. There are Cr_2O_3 oxides and $MnCr_2O_4$ oxides on the

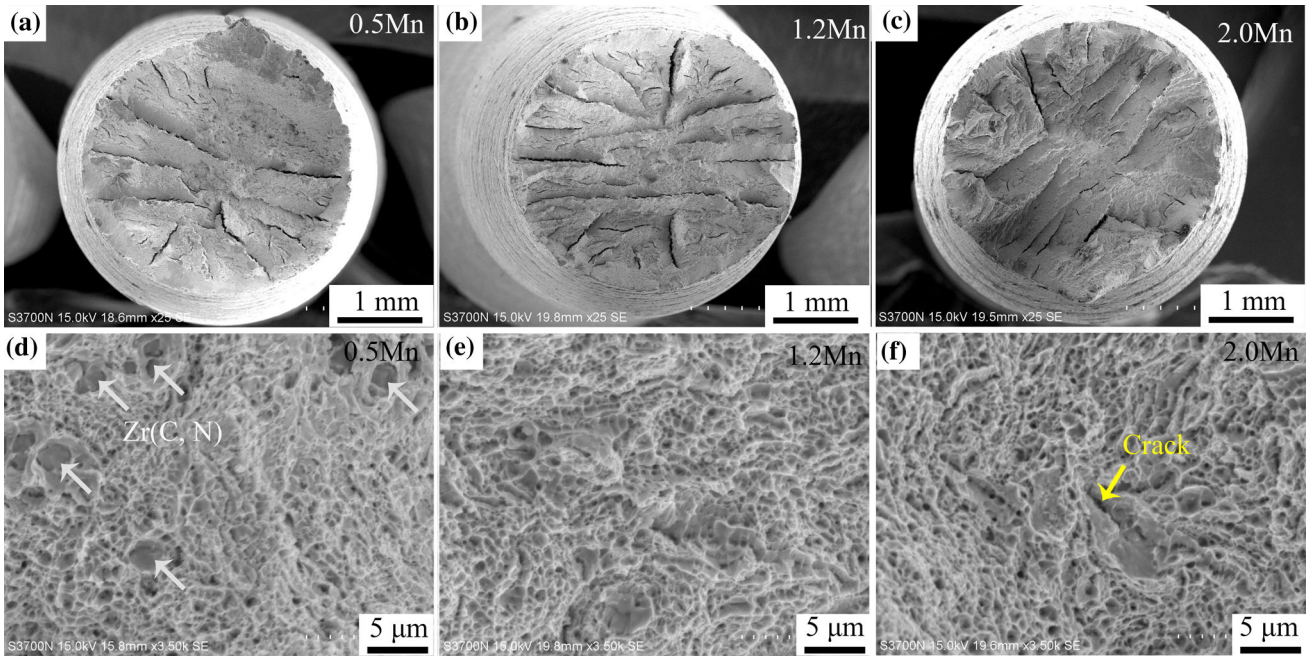

Fig. 9 SEM images of fracture surfaces of (a), (d) 0.5Mn, (b), (e) 1.2Mn, (c), (f) 2.0Mn steels after tensile tests.

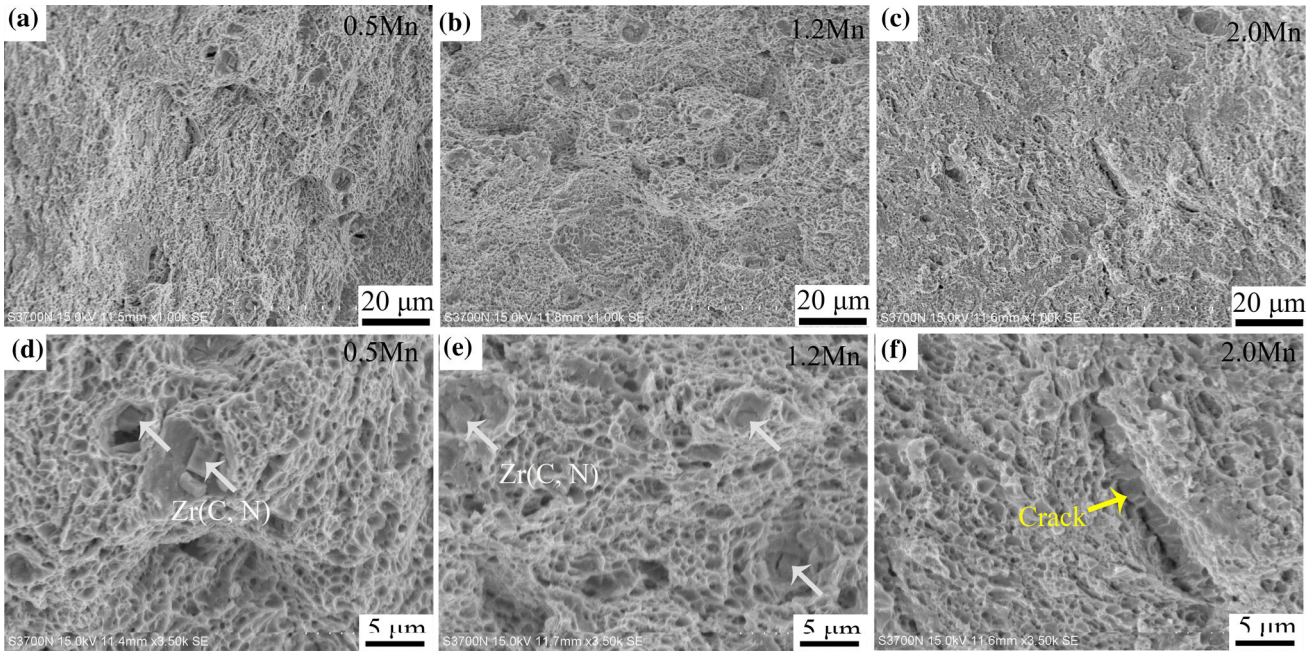

Fig. 10 SEM images of fracture surfaces of (a), (d) 0.5Mn, (b), (e) 1.2Mn, (c), (f) 2.0Mn steels after impact tests.

surface of steels as previous XRD analysis. Therefore, granular oxides and lamellar oxides can be inferred as $MnCr_2O_4$ oxides and Cr_2O_3 oxides, respectively. In addition, there are both Cr_2O_3 oxides and $MnCr_2O_4$ oxides on the surface of 0.5Mn steel according to the previous XRD analysis, while no Cr_2O_3 oxides is observed. This was mainly due to the oxide layers on the steels have shown a two-layer structure: outer layer and inner layer (Ref 39). The $MnCr_2O_4$ oxides are distributed on the outer layer and the Cr_2O_3 oxides are distributed on the inner layer.

The size of granular oxides and lamellar oxides on the surface of the steels were statistically analyzed by image

analysis, and the results are listed in Table 4. The results of average diameter of granular oxides and average length of lamellar oxides were calculated from more than one hundred particles and more than fifty particles, respectively. It can be found that the 1.2Mn steel has the minimum granular oxides with an average diameter of 0.9 ± 0.3 μm. And the 2.0Mn steel has the maximum granular oxides with an average diameter of 1.4 ± 0.4 μm. For lamellar oxides, the average length of 2.0Mn steel is 10.4 ± 2.3 μm, which is ~ 7 times higher that of 1.2Mn steel. Therefore, the reason for 1.2Mn steel exhibits the excellent oxidation resistance could be ascribed to the finer oxides formed on the surface. The finer oxides contribute to form a compactness oxide layer, which improving the oxidation resistance of the steel.

It is found that the oxidation resistance of the steels increases with the Mn content increases from 0.5 to 1.2 wt.%. The reason for this increase could be ascribed to the addition of Mn promotes the formation of Mn oxides (Ref 26), which refined the diameter of granular $MnCr_2O_4$ oxides. However, the oxidation resistance of steels dramatically decreased as the Mn content further increased to 2.0 wt.%. This was mainly because the presence of higher Mn content reduces the critical concentration of Cr to form Cr oxides (Cr_2O_3) (Ref 26). Therefore, the Cr_2O_3 oxides are easier to form in 2.0Mn steel. Finally, the size of lamellar Cr_2O_3 oxides on the surface of 2.0Mn steel is much higher than that of 1.2Mn steel.

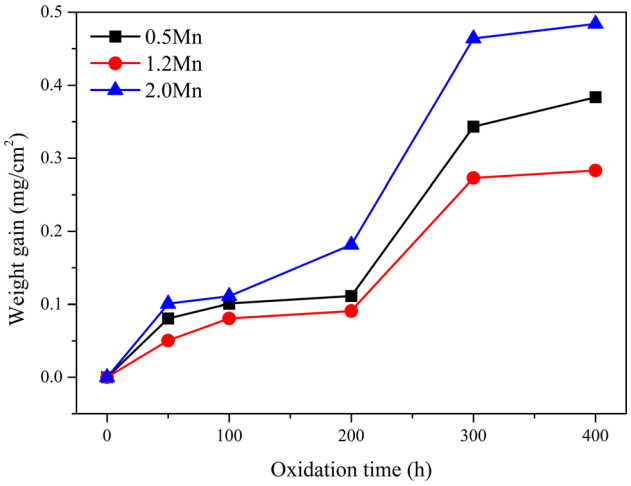

Fig. 11 The plot of weight gain vs. oxidation time of 0.5Mn, 1.2Mn and 2.0Mn steels oxidized at 650 °C for oxidation times ranging from 0 to 400 h.

4. Conclusions

The effect of Mn contents (0.5, 1.2 and 2 wt.%) on the microstructure, mechanical properties and high temperature oxidation resistance of the RAFM steels was systematically investigated. In addition, different normalizing temperatures were carried out in order to optimize its heat treatment process. The major results are summarized as follows:

(1) The optimum normalizing temperature of the RAFM steels is 1040 °C, at which the structure of steels is fully martensite and the hardness of steels is the highest. Except for lath martensite, a large number of $M_{23}C_6$ carbides and a small number of large-sized Zr(C, N) carbonitrides were detected in the steels. The martensitic lath width was refined as the Mn content reaches 2 wt.%. However, the Mn content has little effect on the precipitation behavior of steels.

(2) The strength increases and the toughness decreases with the increase of Mn content. The increase of strength can be ascribed to the solution strengthening by Mn and the gain size strengthening by refining martensitic lath width.

(3) The oxides on the surface of the RAFM steels after oxidation at 650 °C for 400 h are composed of $MnCr_2O_4$ oxides and Cr_2O_3 oxides. The steels with 1.2 wt.% Mn exhibit the optimum high temperature oxidation resistance, followed by steels with 0.5 wt.% Mn. The suitable Mn content is contributed to form fine granular $MnCr_2O_4$ oxides and improve the oxidation resistance of steels. However, the higher Mn content reduces the critical concentration of Cr to form large-sized lamellar Cr_2O_3 oxides and reduces the oxidation resistance of steels.

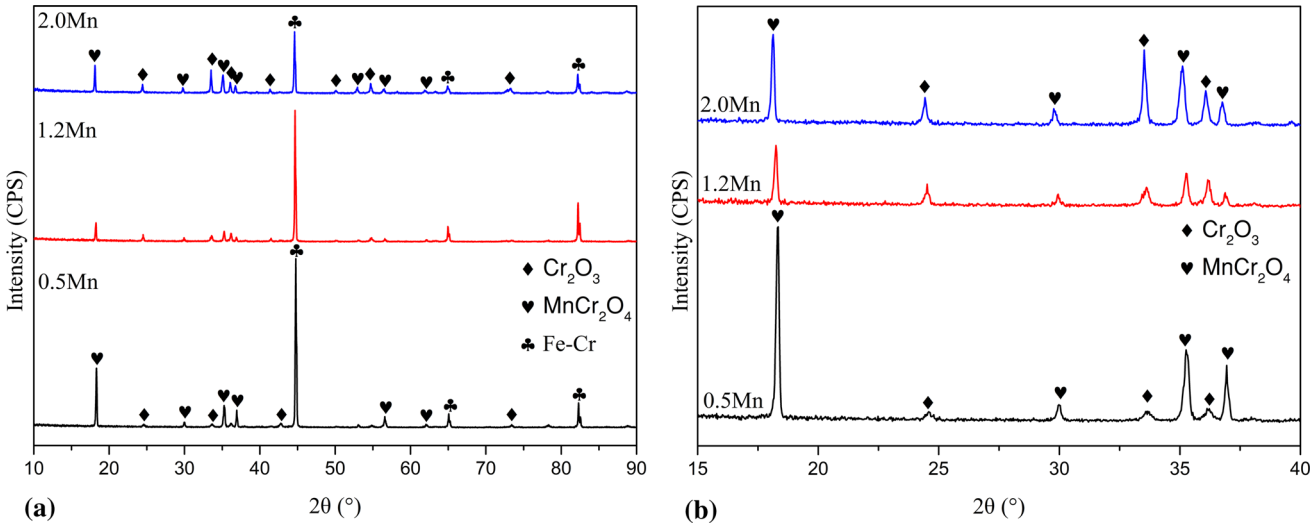

Fig. 12 XRD analysis of the RAFM steels after oxidation at 650 °C for 400 h.

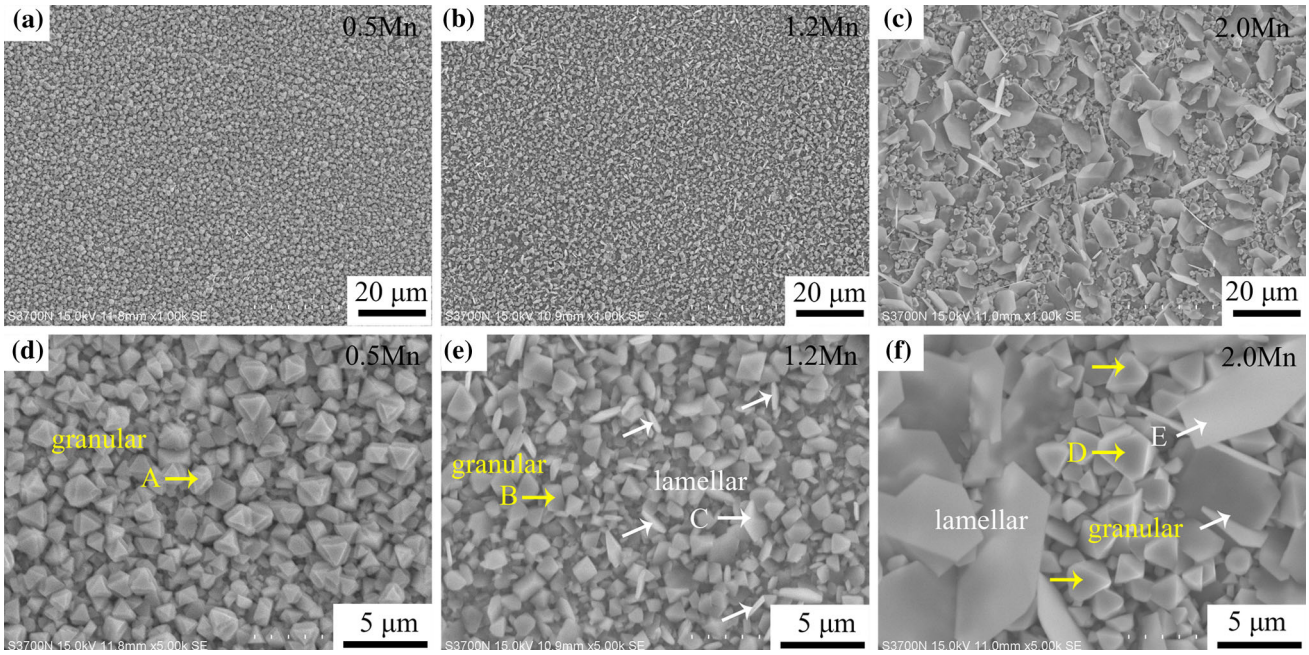

Fig. 13 SEM images showing the surface morphologies of (a, d) 0.5Mn, (b, e) 1.2Mn, (c, f) 2.0Mn steels after oxidation at 650 °C for 400 h.

Table 3 The element content of oxide particles in Fig. 13 by EDS analyses (at.%)

Steels	Oxides	O	Cr	Mn
0.5Mn	A	50.69	25.58	23.73
1.2Mn	B	52.55	28.33	19.13
	C	53.56	40.76	5.68
2.0Mn	D	49.98	28.20	21.82
	E	51.04	38.83	10.13

Table 4 The size of oxides on the surface of the RAFM steels oxidized at 650 °C for 400 h

Steels	Oxides shape	Average diameter/length
0.5Mn	granular	1.2 ± 0.3 μm
1.2Mn	granular	0.9 ± 0.3 μm
	lamellar	1.5 ± 0.3 μm
2.0Mn	granular	1.4 ± 0.4 μm
	lamellar	10.4 ± 2.3 μm

Acknowledgments

This work was supported by the National Natural Science Foundation of China (Grant No. 51421001), the Scientific and Technological Research Program of Chongqing Municipal Education Commission (Grant No. KJQN202201540) and the "111" Project (Grant No. B16007) by the Ministry of Education and the State Administration of Foreign Experts Affairs of China.

References

1. D. Buckthorpe, (2017) Chapter 1-Introduction to Generation IV nuclear reactors, Structural Materials for Generation IV Nuclear Reactorsed., P. Yvon, (Ed.), Woodhead Publishing, Cambridge 1–22
2. Q. Huang, X. Wang, S. Sun, Y. Liu, H. Liao, P. Zheng, L. Peng, and Y. Zhai, Development of Reduced Activation Ferritic/Martensitic Steels in China, *J. Nucl. Mater.*, 2022, **568**, p 153887.
3. Y. Shen, H. Liu, Z. Shang, and Z. Xu, Precipitate Phases in Normalized and Tempered Ferritic/Martensitic Steel P92, *J. Nucl. Mater.*, 2015, **465**, p 373–382.
4. Y. Shen, X. Zhou, X. Huang, Z. Fan, X. Ma, H. Chen, and X. Shi, Identification of Precipitate Phases in CLAM Steel, *Fusion Eng. Des.*, 2021, **163**, p 112168.
5. Y.Z. Shen, S.H. Kim, H.D. Cho, C.H. Han, and W.S. Ryu, Precipitates in Normalized and Tempered 10%Cr Ferritic/Martensitic Steels, *J. Nucl. Mater.*, 2012, **430**(1–3), p 264–269.
6. S. Ge, B. Niu, Z. Wang, Q. Pan, C. Liu, and Q. Wang, Microstructural Stability and Mechanical Property of a Medium-Si 12%Cr Reduced Activation Ferritic/Martensitic Steel at High Temperatures, *J. Mater. Eng. Perform.*, 2022, **31**(7), p 5697–5705.
7. Q. Min, Q. Guo-xing, C. Ming-chong, D. Qing, C. Lei, and W. Hong-yan, Microstructure Stability and Mechanical Properties of Reduced Activated Ferritic Martensitic Steel during Thermal Aging at 550 °C for 5000 h, *J. Mater. Eng. Perform*, 2022 https://doi.org/10.1007/s11665-022-07498-6
8. L. Zhao, X. Chen, T. Wu, and Q. Zhai, Study on Strengthening Mechanism of 9Cr-1.5Mo-1Co and 9Cr-3W-3Co Heat Resistant Steels, *Materials*, 2020, **13**(19), p 4340.
9. J.H. Zhou, Y.F. Shen, and N. Jia, Strengthening Mechanisms of Reduced Activation Ferritic/Martensitic Steels—A Review, *Int. J. Miner. Metall. Mater.*, 2021, **28**(3), p 335–348.
10. S.F. Yang, M.J. Zhao, J. Feng, J.S. Li, and C.S. Liu, Induced-Pitting Behaviors of MnS Inclusions in Steel, *High Temp. Mater. Proc.*, 2018, **37**(9–10), p 1007–1016.
11. H. Yu, M. Li, J. Zhang, and D. Yang, Effect of Mn Content on the Reaction between Fe-xMn (x = 5, 10, 15, and 20 Mass pct) Steel and CaO-SiO_2-Al_2O_3-MgO Slag, *Metals*, 2021, **11**(8), p 1200.
12. C.L. Zhang, H.G. Fu, S.Q. Ma, D.W. Yi, J. Lin, Z.G. Xing, and Y.P. Lei, Effect of Mn Content on Microstructure and Properties of Wear-Resistant Bainitic Steel, *Mater. Res. Exp.*, 2019, **6**(8), p 086581.
13. T. Zhao, F. Wang, C. Chen, H. Ma, Z.A. Yang, F.C. Zhang, and T.B. Tang, Effect of Mn Content and Strain Rate on Mechanical Properties of High-C High-Mn Austenitic Steel, *Mater. Sci. Eng. A.*, 2022, **851**, p 143653.
14. M. Schulte, S. Steentjes, N. Leuning, W. Bleck, and K. Hameyer, Effect of Manganese in High Silicon Alloyed Non-Oriented Electrical Steel Sheets, *J. Magn. Magn. Mater.*, 2019, **477**, p 372–381.

15. J.B. Li, X.Y. Xiong, Q. Shen, Q.K. Zhai, and W.Q. Liu, Effect of Mn on precipitation behaviour of NiAl phase in Fe-NiAl steels, *Mater. Sci. Technol.*, 2020, **36**(7), p 852–857.
16. Q. Shen, X.J. Wang, A.Y. Zhao, Y.F. He, X.L. Fang, J.R. Ma, and W.Q. Liu, Effects of Mn on Multi-Precipitates Evolution of Cu-Rich and Nial Phase in Steels, *Acta Metall. Sin.*, 2016, **52**(5), p 513–518.
17. J. Oñoro, Martensite Microstructure of 9–12%Cr Steels Weld Metals, *J. Mater. Process. Technol.*, 2006, **180**, p 137–142.
18. P. Hu, W. Yan, L.-F. Deng, W. Sha, Y. Shan, and K. Yang, Nitride-Strengthened Reduced Activation Ferritic/Martensitic Steels, *Fusion Eng. Des.*, 2010, **85**, p 1632–1637.
19. C.-H. Lee, J. Moon, M.-G. Park, T.-H. Lee, M.-H. Jang, H.C. Kim, and D.-W. Suh, Effect of Constituent Phase on Mechanical Properties of 9Cr–1WVTa Reduced Activation Ferritic–Martensitic Steels, *J. Nucl. Mater.*, 2014, **455**(1), p 421–425.
20. W. Zeng, M. Zhou, M. Yang, and R. Qiu, Effect of Zr on the Microstructure and Mechanical Properties of 12Cr Ferritic/Martensitic Steels, *Fusion Eng. Des.*, 2022, **177**, p 113084.
21. J. Wang, K. Zhu, J. Zhou, and X. Lu, Effects of Peak Temperatures and Cooling Rates on Delta Ferrite Formation and Mechanical Properties for Heat Affected Zones in 9Cr-RAFM Steel, *Int. J. Press. Vessel Pip.*, 2021, **192**, p 104399.
22. Z. Shang, Y. Shen, B. Ji, and L. Zhang, Effect of δ-Ferrite Evolution and High-Temperature Annealing on Mechanical Properties of $11Cr_3W_3Co$ Ferritic/Martensitic Steel, *Met. Mater. Int.*, 2016, **22**(2), p 171–180.
23. W.C. Zhong, Y. Yang, K.G. Field, N. Sridharan, K. Terrani, and L.Z. Tan, Microstructure and Mechanical Properties of High Mn-Containing Ferritic-Martensitic Alloys Exposed to Cyclical Thermal Treatment, *Mater. Sci. Eng. A.*, 2021, **813**, p 141143.
24. S. Chen, X. Jin, and L. Rong, Improvement in High Temperature Oxidation Resistance of 9%Cr Ferritic–Martensitic Steel by Enhanced Diffusion of Mn, *Oxid. Met.*, 2016, **85**(1), p 189–203.
25. S.H. Chen, and L.J. Rong, Roles of Mn in the High-Temperature Air Oxidation of 9Cr Ferritic-Martensitic Steel After Severe Plastic Deformation, *Oxid. Met.*, 2018, **89**(3–4), p 415–428.
26. X. Jin, S. Chen, and L. Rong, Effects of Mn on the Mechanical Properties and High Temperature Oxidation of $9Cr_2WVTa$ Steel, *J. Nucl. Mater.*, 2017, **494**, p 103–113.
27. Z. Dong, M. Li, Y. Behnamian, J.-L. Luo, W. Chen, B.S. Amirkhiz, P. Liu, X. Pang, J. Li, W. Zheng, D. Guzonas, and C. Xia, Effects of Si, Mn on the Corrosion Behavior of Ferritic–Martensitic Steels in Supercritical Water (SCW) Environments, *Corros. Sci.*, 2020, **166**, p 108432.
28. J. Gong, H. Liao, K. Zhang, and X. Wang, Heat Treatment Optimization of China Low-Activation Ferritic/Martensitic Steel with Cerium Addition, *Fusion Eng. Des.*, 2020, **158**, p 111696.
29. L. Yang, F. Zhao, and W. Ding, Laves Phase Evolution in China Low-Activation Martensitic (CLAM) Steel during Long-Term Aging at 550 °C, *Materials.*, 2019, **13**, p 154.
30. H.K. Danielsen, Review of Z Phase Precipitation in 9–12 wt.-%Cr Steels, *Mater. Sci. Technol.*, 2016, **32**(2), p 126–137.
31. L. Cipolla, H.K. Danielsen, D. Venditti, P.E. Di Nunzio, J. Hald, and M.A.J. Somers, Conversion of MX Nitrides to Z-Phase in a Martensitic 12% Cr Steel, *Acta Mater.*, 2010, **58**(2), p 669–679.
32. Y. Shen, X. Zhou, T. Shi, X. Huang, Z. Shang, W. Liu, B. Ji, and Z. Xu, Sigma Phases in an 11%Cr Ferritic/Martensitic Steel with the Normalized and Tempered Condition, *Mater. Charact.*, 2016, **122**, p 113–123.
33. T.N. Baker, Role of Zirconium in Microalloyed Steels: A Review, *Mater. Sci. Technol.*, 2015, **31**(3), p 265–294.
34. C. Qiu, H.S. Zurob, and C.R. Hutchinson, The Coupled Solute Drag Effect During Ferrite Growth in Fe-C-Mn-Si Alloys Using Controlled Decarburization, *Acta Mater.*, 2015, **100**, p 333–343.
35. V.K. Devra and J. Maity, Solute Drag Effect on Austenite Grain Growth in Hypoeutectoid Steel, *Philos. Mag. Lett.*, 2020, **100**(6), p 245–259.
36. H. Bhadeshia and R. Honeycombe, Chapter 15-Modelling of Structure and Properties, Steels: Microstructure and Properties (Fourth Edition) ed., H. Bhadeshia, R. Honeycombe. Butterworth-Heinemann, Oxford 421–455 (2017)
37. M. Song, C. Sun, Z. Fan, Y. Chen, R. Zhu, K.Y. Yu, K.T. Hartwig, H. Wang, and X. Zhang, A Roadmap for Tailoring the Strength and Ductility of Ferritic/Martensitic T91 Steel Via Thermo-Mechanical Treatment, *Acta Mater.*, 2016, **112**, p 361–377.
38. J.T. Ju, Y. Wang, F. Hao, Y.X. Du, W. Jiang, and F. Sun, Effect of Silicon on Mechanical Properties of Ti-6AI-2Zr-1Mo-1V Alloy, *Rare Met. Mater. Eng.*, 2019, **48**, p 1749–1755.
39. L. Zhang, W. Yan, Q. Shi, Y. Li, Y. Shan, and K. Yang, Silicon Enhances High Temperature Oxidation Resistance of SIMP Steel at 700 °C, *Corros. Sci.*, 2020, **167**, p 108519.